The 5 April 2024 Mw 4.8 Tewksbury, New Jersey aftershock sequence resolved with machine-learning-enhanced detection methods

Eric Beaucé[1], Felix Waldhauser[1], David Schaff[1], Won-Young Kim[1], and Folarin Kolawole[1]

[1]Lamont-Doherty Earth Observatory, Columbia University

February 14, 2025

The Ramapo Seismic Zone (RSZ) in the Northeastern United States hosts frequent but poorly understood intraplate earthquakes, potentially posing a significant hazard to the nearby New York metropolitan area. The 5 April 2024, M_w4.8, Tewksbury, New Jersey earthquake, provides a rare opportunity to study the RSZ seismicity. We applied machine-learning-enhanced backprojection, matched-filtering, correlation-timing and double-difference methods to continuous waveforms recorded at local and regional stations to detect and locate about 2,000 aftershocks ($M_w > 0.0$) within the 74 days following the mainshock. They reveal a single, 51^o east-southeast dipping fault plane possibly abutting the Ramapo fault at depth to the north. Aftershock locations are consistent with a shallow ($\sim$ 4km) mainshock hypocenter with rupture propagating downward and terminating at a depth of about 6km. A relatively high Gutenberg-Richter b-value ($b \approx 1.19$) and a low aftershock spatial fall-off rate ($\gamma \approx 1.8$) suggest that the Tewksbury sequence activated a rough, immature fault.

The 5 April 2024 M_w4.8 Tewksbury, New Jersey aftershock sequence resolved with machine-learning-enhanced detection methods

Eric Beaucé[1], Felix Waldhauser[1], David Schaff[1], Won-Young Kim[1], Folarin Kolawole[1]

[1]Lamont-Doherty Earth Observatory, Columbia University

Key Points:

- We detected and located 2,027 aftershocks over 74 days using machine-learning-enhanced techniques and double-difference methods.
- A 51.0±2.0° east-southeast dipping fault was activated by the seismic sequence, next to the Ramapo fault and possibly interacting with it.
- The Gutenberg-Richter *b*-value, $b = 1.19$, and the aftershock spatial characteristics suggest the immaturity and complexity of the fault.

Corresponding author: Eric Beaucé, `ebeauce@ldeo.columbia.edu`

Abstract

The Ramapo Seismic Zone (RSZ) in the Northeastern United States hosts frequent but poorly understood intraplate earthquakes, potentially posing a significant hazard to the nearby New York metropolitan area. The 5 April 2024, M_w4.8, Tewksbury, New Jersey earthquake, provides a rare opportunity to study the RSZ seismicity. We applied machine-learning-enhanced backprojection, matched-filtering, correlation-timing and double-difference methods to continuous waveforms recorded at local and regional stations to detect and locate about 2,000 aftershocks ($M_w > 0.0$) within the 74 days following the mainshock. They reveal a single, 51° east-southeast dipping fault plane possibly abutting the Ramapo fault at depth to the north. Aftershock locations are consistent with a shallow (~ 4 km) mainshock hypocenter with rupture propagating downward and terminating at a depth of about 6 km. A relatively high Gutenberg-Richter b-value ($b \approx 1.19$) and a low aftershock spatial fall-off rate ($\gamma \approx 1.8$) suggest that the Tewksbury sequence activated a rough, immature fault.

Plain Language Summary

Northeastern America has been shaken by intermediate-size earthquakes (magnitudes approximately 5) several times in the last century, and a repeat of the 1755 Cape Ann, Massachusetts event (magnitude estimated to be about 6), or of the 2011 magnitude 5.8 (M_w) Mineral, Virginia earthquake, has disastrous potential for typical urban infrastructure in this region. On Friday, April 5, 2024, at 10:23am local time, a magnitude 4.8 (M_w), oblique thrust earthquake struck near Tewksbury, New Jersey. It was the first earthquake that strong to occur within 65 km (40 miles) of New York City since 1884. In this study, we analyzed 74 days of seismic data recorded by a local network of 26 seismometers that were rapidly deployed by several institutions following the M_w4.8 earthquake. Our results show that the Tewksbury earthquake and most of the over 2,000 aftershocks occurred on a small, well-defined fault located in the Ramapo seismic zone, about 5 km away from the main surface strand of the Ramapo fault. The aftershock statistical properties suggest the sequence activated a young, immature fault.

1 Introduction

The Ramapo seismic zone (RSZ) hosts frequent, weak intraplate seismicity (earthquake magnitudes smaller than 3) in the Northeastern United States (US). Most of these earthquakes are caused by thrust faulting indicating northeast-southwest compression and occur near, rather than on, the Ramapo fault itself, which is misoriented for slip within the contemporary stress field (Page et al., 1968; Sykes et al., 2008). Thus, these earthquakes result from the failure of more favorably oriented faults within the RSZ, but the forces driving them are still poorly understood. On 5 April 2024, at 10h23 local time (14h23 Coordinated Universal Time, UTC), a magnitude (M_w) 4.8 earthquake struck in the RSZ near the town of Tewksbury in New Jersey, US, about 65 km (40 miles) from New York City. The intermediate-size, oblique thrust event (Han et al., 2024, see Figure 1) marked the beginning of a several-month-long period of elevated seismic activity. The largest aftershock (M_w3.7) occurred 7.5 hours later and a single foreshock (m_b2.2) was reported on 14 March 2024 by the US Geological Survey (USGS). The closest operational seismic station, LD.PAL, located on the Lamont-Doherty Earth Observatory (LDEO) campus, was about 80 km away from the mainshock epicenter, making it difficult to monitor in detail the early development of the earthquake sequence. Several institutions – LDEO, USGS, Texas Seismological Network (TexNet), and Yale and Rutgers Universities (Boyd et al., 2024) – deployed a total of 26 temporary stations over the course of a few days to weeks, recording the seismic sequence in increasingly greater detail.

The Ramapo seismic zone, like the rest of Eastern US, is located in a stable continental region (SCR), that is, a region away from active plate boundaries where geodetically observed strain rates are below noise levels (Craig & Calais, 2014), raising the question as to what drives seismicity (Armbruster & Seeber, 1987; Seeber et al., 2002; Calais et al., 2016). Despite the absence of significant tectonic forcing, large earthquakes do occur in SCRs, like the 2017 M_w6.5 Botswana event (Gardonio et al., 2018) or the 1811-1812 New Madrid sequence of four M_w7.0 to 7.5 earthquakes (Johnston & Schweig, 1996). It has been shown that exceedingly small stress perturbations ($\sim$1 kPa) can affect the rates of seismicity (Heki, 2003; Frank et al., 2016; Craig et al., 2017; Beaucé et al., 2023). Thus, possible drivers of seismicity in SCRs include different types of environmental forcing such as seasonal hydrological (Bollinger et al., 2007; Craig et al., 2017; Johnson et al., 2017) and snow (Heki, 2003) loading, the solid Earth tides (Delorey et al., 2017; Beaucé et al., 2023) and, particularly in the Northeastern US, stresses caused by glacial isostatic adjustment (Wu & Johnston, 2000). Moreover, anthropogenic activity like mining can cause minor stress perturbations in the shallow crust and may contribute to causing seismicity (Pomeroy et al., 1976; Seeber et al., 1998).

The scarcity of intermediate-size earthquakes and sparse station coverage typically prevent the detailed study of these events and the unambiguous identification of the causative faults (Kafka et al., 1985). The 2024 Tewksbury earthquake sequence, and the data it generated, offer a unique opportunity to image active tectonic structures within the RSZ with unprecedented resolution. We analyzed the continuous waveforms from both permanent and temporary stations with machine-learning and waveform-correlation based earthquake detection techniques (Beaucé et al., 2024) to build a catalog of 2,027 aftershocks over 10 weeks of local monitoring. The new catalog sheds light on seismogenesis in the RSZ and on the possible interplay between young secondary faults and the ancient main strand of the Ramapo fault, and the potential hazard these faults pose to the nearby New York metropolitan region.

2 Data

We analyzed the seismic data recorded by 42 stations between 2024-04-05 and 2024-06-18. These stations include 16 instruments from the permanent, regional networks LD, PE, N4 and NE and 26 instruments from temporary, local networks (LD, GS and 4N) deployed by several institutions in the days that followed the mainshock (see Section 7). Unfortunately, the permanent station closest to the mainshock and largest aftershock, LD.BRNJ, was not operating on the day they occurred, but was repaired 4 days later, together with other nearby stations (LD.PANJ, LD.ODNY). Figure 1 shows the locations of the seismic stations as well as their data availability over time. The permanent stations sample at 100 Hz while the temporary stations include broadband stations sampling at 100 Hz (GS and one 4N deployed by TexNet) and short-period stations sampling at 250 Hz (4N deployed by TexNet) and 500 Hz (LD.RAMPX deployed by LDEO and 4N deployed by Rutgers and Yale universities). We bandpass filtered the data between 2 Hz and 20 Hz for earthquake detection and between 2 Hz and 48 Hz for phase picking (see Text S1.1). The data were resampled at 100 Hz.

3 Methodology

We processed the continuous seismic data with the automated earthquake detection and location workflow BackProjection and Matched-Filtering (BPMF, Beaucé et al., 2024). The workflow is organized in two stages where, first, an initial earthquake catalog is built using a machine-learning-(ML)-enhanced (PhaseNet, Zhu & Beroza, 2019) backprojection technique and, then, using the initially detected earthquakes as templates for a matched-filter search to detect mostly smaller events missed during the first stage. Earthquake locations were determined using the first P- and S-wave arrivals picked by PhaseNet and the location software NLLoc (Lomax et al., 2009). We optimized the equal differential time likelihood function in NLLoc to mitigate the presence of outliers in the automatic picks. P- and S-wave travel time tables were computed by solving the Eikonal equation (White et al., 2020) in a 1D layered crustal model for the region (Yang & Aggarwal, 1981). For more details on BPMF see also Beaucé et al. (2019, 2022, 2024).

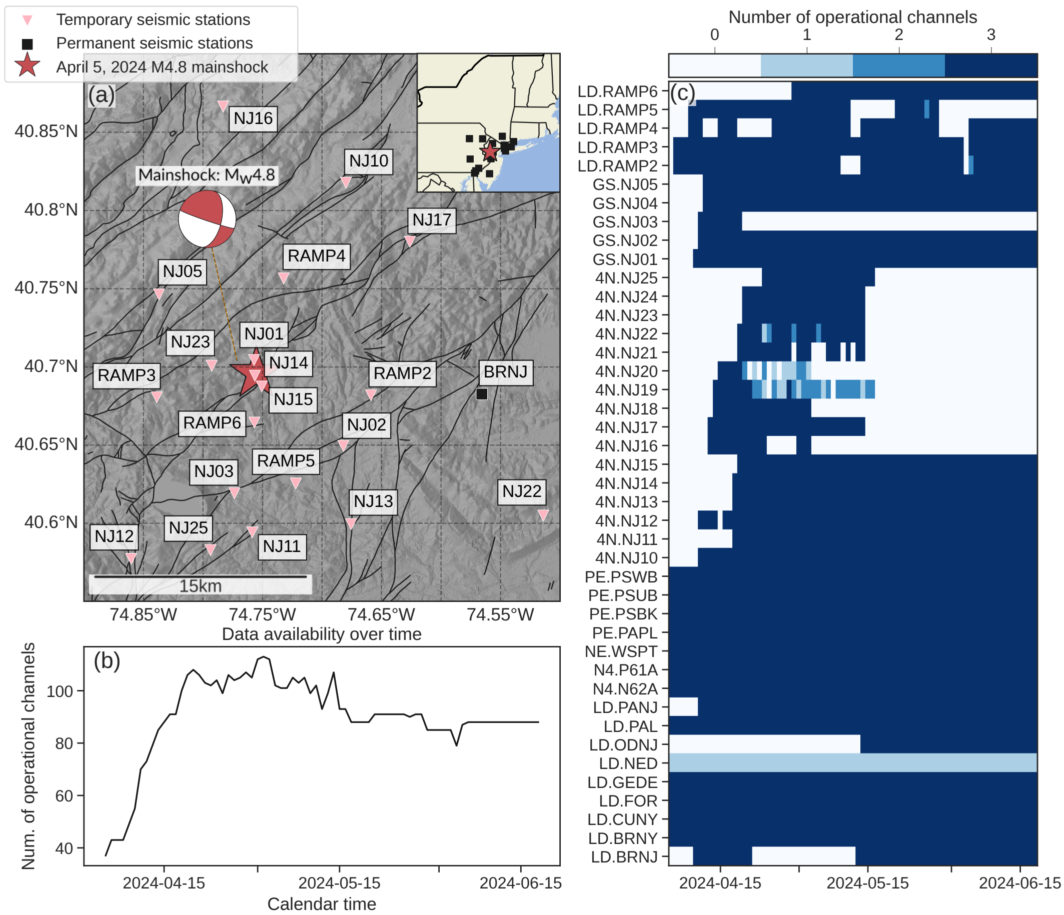

Figure 1. **(a)** Map of the seismic stations used in this study and mainshock focal mechanism (from Han et al., 2024, strike: 13±0.9°, dip: 45±4.0°, rake: 172±1.3°). The regional, permanent networks LD, PE, N4 and NE were supplemented by the local, temporary networks LD.RAMPX, GS and 4N (see Section 7). **(b)** Total number of operational seismic channels over time. **(c)** Number of operational channels per seismic station over time. Data availability may have improved since the time of the study.

The catalog of earthquakes, with quarry blasts removed (see Text S1.2), is then relocated using the double-difference method HypoDD (Waldhauser & Ellsworth, 2000; Waldhauser, 2001) together with the PhaseNet picks and precise phase delay times between nearby events (< 5 km) computed by cross-correlating seismograms at common stations (Schaff et al., 2004). The time-domain cross-correlation measurements were performed on filtered seismograms (1-15 Hz) with 0.45 s and 1.0 s long windows for P- and S-phases, respectively (see also Waldhauser & Schaff, 2008). More details on HypoDD parameters are given in Text S1.3.

Earthquake moment magnitudes M_w were estimated by fitting the Boatwright model (Boatwright, 1978) to the S-wave displacement spectrum computed using the multi-band-pass filtering approach described in Al-Ismail et al. (2023). We corrected for the anelastic attenuation of seismic waves using the frequency-dependent quality factor $Q = 750f^{0.24}$, which is an average value for the attenuation of shear waves in the Northeastern US (J. Shi et al., 1996, 1997). More details on displacement spectrum computation and modeling are given in Text S2.1. Signal-to-noise ratio (SNR) limitations prevented us from fitting the Boatwright model to the S-wave displacement spectrum for most of the smaller events. For those, we computed an approximate moment magnitude, M_{w^*}, using the highest SNR frequency bands of the spectrum (see Text S2.3). We validated our approximate moment magnitudes against full moment magnitudes and the USGS magnitudes (see Figure S3). We modeled the magnitude distribution with the Gutenberg-Richter law (Gutenberg & Richter, 1941) and computed the maximum likelihood estimate of the b-value (Aki, 1965) as well as its error following Y. Shi and Bolt (1982). To compute the b-value, we estimated the magnitude of completeness M_c using the maximum curvature technique (Wiemer & Katsumata, 1999). We then added 0.2 to M_c to further prevent errors in M_c from propagating into the b-value estimate.

4 Results

Using BPMF (Beaucé et al., 2024), we detected and located 2,027 earthquakes over the 74 days in the study area (Figure 2a). Of the 2,027 events, 838 were detected and located in the initial ML-enhanced backprojection stage using the 6 seismic stations closest to each test source of the grid, with a median epicentral error of 0.46 km. Using these events as templates in a matched-filter search over the 10 seismic stations that have the highest SNR for each template, we found an additional 1,189 events. In comparison, the USGS reported 195 earthquakes over the same time period (see Section 7). Event magnitudes range from M_{w^*} 0.0-4.8, with a magnitude of completeness $M_c = 0.72$ and a b-value of $b = 1.19 \pm 0.03$ (Figure 2b). At this stage, most events detected with matched-filtering were too small for phase picking and could not be located independently from their template (1,025 out of 2,027 events). For these events, the correlation delay times constrained their relative location during double-difference analysis of the entire catalog.

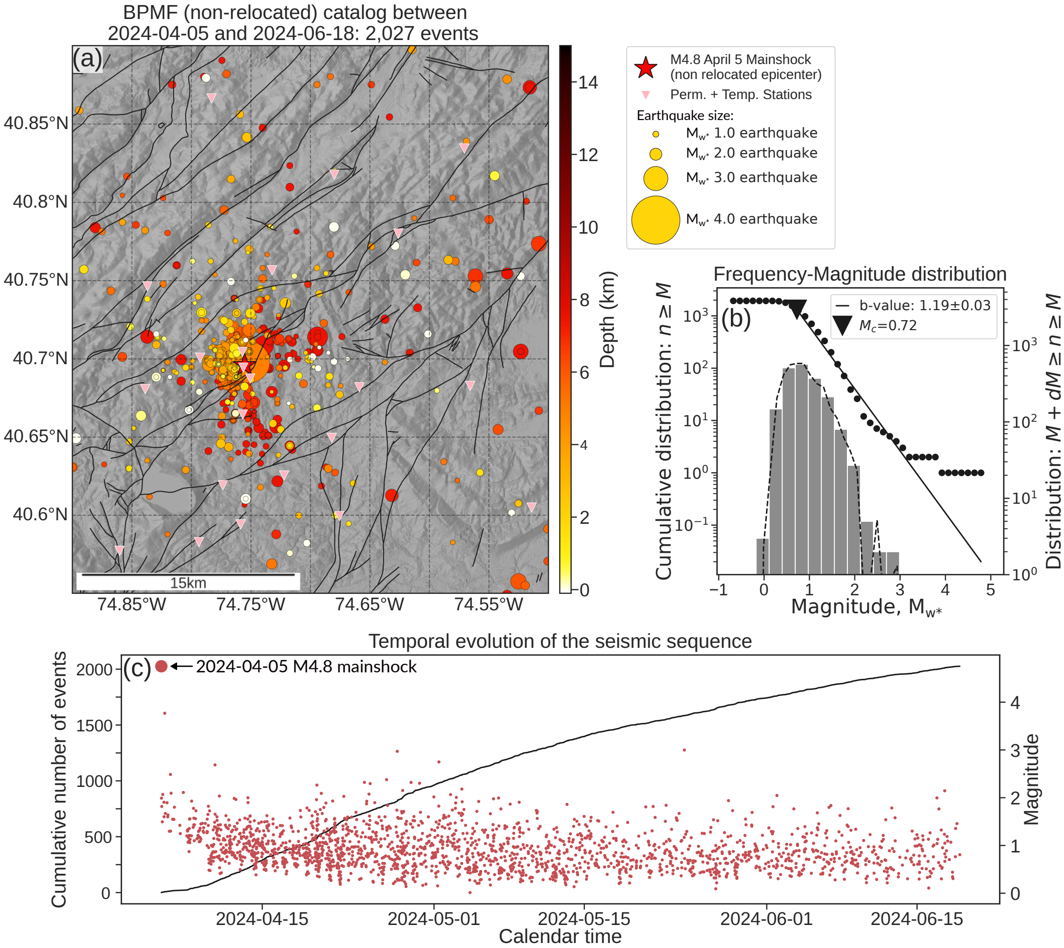

Figure 2. **(a)** Map view of the 2,027 earthquakes detected and located with BPMF. **(b)** Distribution of earthquake magnitudes with cumulative count (left axis) and count (right axis). **(c)** Cumulative number of detected earthquakes and earthquake magnitudes as a function of time.

In the days following the mainshock, the detection rate increased due to the deployment of local stations (Figure 1) that were able to record smaller events (Figure 2c). The highly temporally variable network makes it difficult to interpret the detection rate in terms of seismicity rate. Nonetheless, the seismic activity seems to decay more slowly compared to the canonical Omori-like aftershock rate decay, $n(t) \sim t^{-p}$, with $p \approx 1$

(Ōmori, 1894; Utsu et al., 1995). Focusing on earthquakes with magnitudes well above the 74-day M_c using cut-off minimum magnitudes ranging from 1.25 to 2.00 yields estimates of p ranging from 0.25 to 0.80 (see Figure S4).

The average horizontal and vertical location 1-sigma uncertainties for the NLLoc locations are 1.1 km and 0.49 km, respectively, and root-mean-square (RMS) travel-time residual of 0.08 s. These uncertainties are mostly due to errors in the phase picks and the velocity model used for locating the events. Relocation of the initial catalog using double-differences, which minimizes both sources of errors (Waldhauser & Ellsworth, 2000), results in a high-resolution catalog of 1,738 events (see Figure 3) with median, bootstrap derived, relative location uncertainties of 22 m in horizontal and 17 m in vertical directions. A total of 4,464,441 P- and 4,067,925 S-wave cross-correlation delay times with correlation coefficients 0.7 or higher were used in the inversion. We fitted a fault plane to the $M_{w^*} > 1.75$ earthquake hypocenters near the mainshock and found a N6.4±4.4° trending plane, dipping 51.0±2.0° to the ESE. Aftershocks are distributed around the fault but most occur on the fault plane itself (Figure 3b, c).

We analyzed the spatial distribution of the aftershocks by measuring the power-law fall-off rate of event density as a function of distance from the fault (Powers & Jordan, 2010; T. Goebel et al., 2014; Perrin et al., 2021). We divided the data into hanging wall and foot wall seismicity and estimated the fall-off rate using the maximum likelihood estimate (Clauzet et al., 2009; T. Goebel et al., 2014, see Figure 3d and Text S4). Estimates were made using data at distances larger than 0.2 km, which represents the width of the deformation zone associated with the main fault (Powers & Jordan, 2010; Perrin et al., 2021). This minimum cut-off distance was chosen based on the stability of the estimates around it (see Figure S5). Because of the lack of events further than 10 km from the fault, mainly due to the finite width of the seismogenic zone, the power-law behavior cannot be observed beyond 10 km and this upper truncation induces concavity

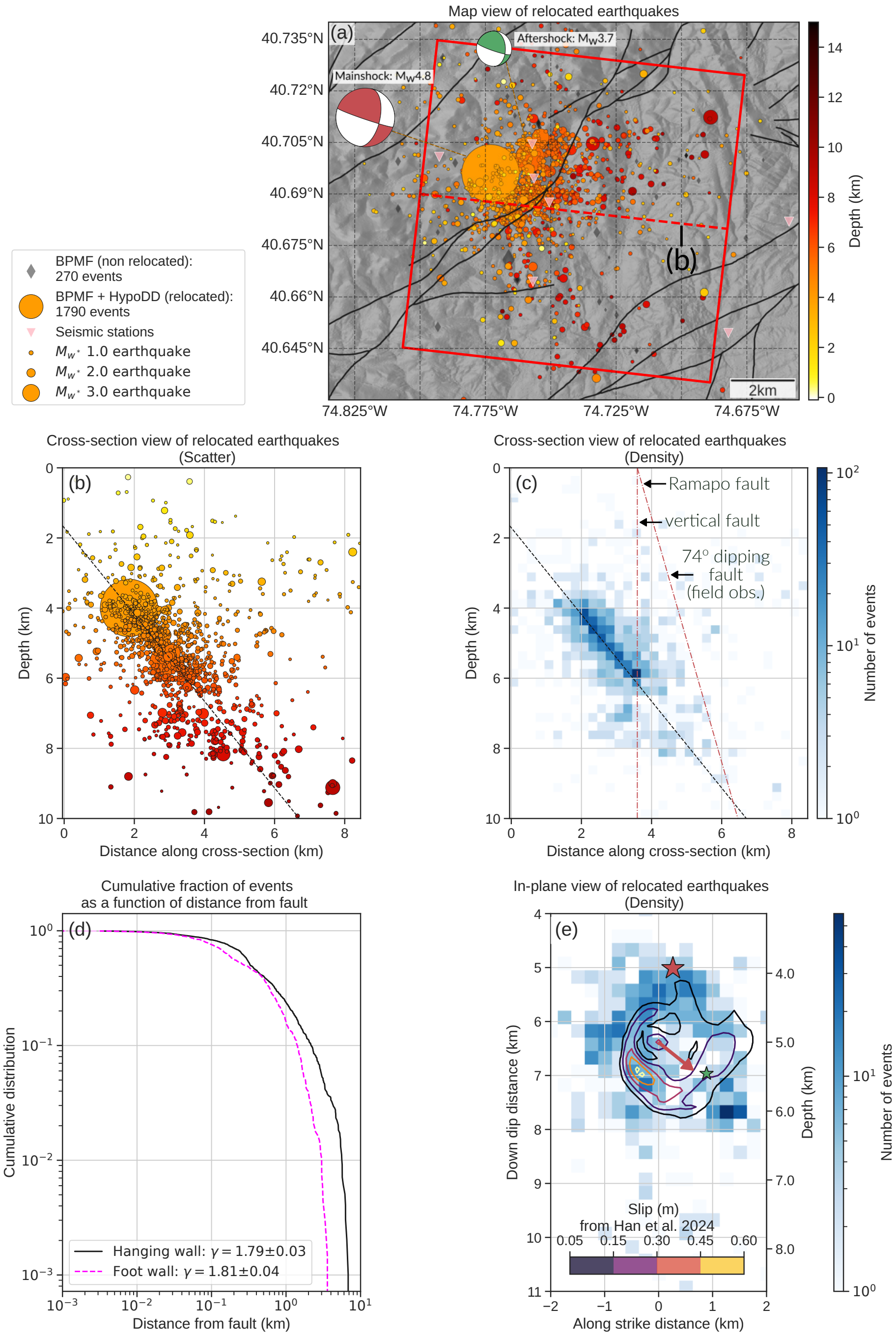

Figure 3. **(a)** Map of double-difference relocated earthquakes. Depth is color-coded and symbol size scales with magnitude. Beachballs show the mainshock and the $M_w3.7$ aftershock focal mechanisms (Han et al., 2024). **(b)** Along-dip cross-section. The black dashed line shows the best fitting plane for $M_{w*} > 1.75$ earthquake hypocenters near the mainshock. **(c)** Same as (b) but with event density. The red dashed lines show the depth continuation of the Ramapo fault using vertical and 74° (Kolawole et al., under review) dips. **(d)** Cumulative fraction of events located further than a given distance from the fault. The power-law fall-off rate, γ, is given by the maximum likelihood estimate for distances above 0.2 km. **(e)** Density of hypocenters orthogonally projected onto the fault plane, measured in 250 m×250 m cells using hypocenters less than 500 m away from the plane. Slip contours are from Han et al. (2024). The red star shows the mainshock hypocenter (rupture initiation) and the green star shows the $M_w3.7$ aftershock hypocenter.

at the tip of the cumulative distribution (Burroughs & Tebbens, 2001, see Figure 3d). Our estimates yield similar fall-off rates $\gamma = 1.80 \pm 0.05$ for the hanging and foot walls.

5 Discussion

5.1 Aftershock Distribution and Fault Structure

Aftershock locations image a previously unmapped east-southeast dipping fault adjacent to the Ramapo fault (Figure 3). Its up-dip continuation reaches the surface near the town of Mountainville, New Jersey, and is hereafter named the Mountainville fault (Kolawole et al., under review). The mainshock hypocenter was relocated at 4.0 km depth (Figure 3), deeper than reported by the USGS (2.6 km). The hypocenter represents the nucleation location as derived from the phase arrival onset. The aftershock distribution (Figure 3e) suggests that the mainshock broke a relatively small fault area of $A_m \approx 2\,\text{km}^2$ between 4 km and 6 km depth, supporting a downward propagating rupture consistent with results from waveform modeling (Han et al., 2024). The largest aftershock, M_w3.7, was relocated at 5.5 km depth in an area of low aftershock productivity (Figure 3e). Main slip area, depth range and fault orientation (N6.4±4.4° trending plane, dipping 51.0±2.0° to the ESE) derived in this study from aftershock locations agree well with those inferred from waveform modeling (Han et al., 2024, see Figure 1) and with the orientation of paleo-slip surfaces observed in outcrops near Mountainville (Kolawole et al., under review).

Han et al. (2024) approximated their rupture area as a r=1.1 km-radius circular crack and estimated a static stress drop of $\Delta\sigma \approx 6.6\,\text{MPa}$ ($\Delta\sigma = (7/16)M_0/r^3$, Eshelby, 1957). However, the aftershock data cannot rule out smaller slip areas, implying that stress drop could be larger. For example, for $r_m = \sqrt{A_m/\pi} \approx 800\,\text{m}$, stress drop is $\Delta\sigma \approx 17\,\text{MPa}$. Moreover, assuming a corner frequency $0.50\,\text{Hz} < f_c < 1.0\,\text{Hz}$, based upon the observations in Han et al. (2024, their Figure 2c), using their parameters (S-wave speed V_s=3400 m/s and rupture speed V_r=1870 m/s), we calculate a wide range of stress drops $\Delta\sigma$ = 13-104 MPa using the Madariaga model ($r = kV_r/(2\pi f_c)$, $k =$

1.47, Madariaga, 1976) and $\Delta\sigma = 2.3\text{-}18\,\text{MPa}$ using the Brune model ($k = 2.62$, Brune, 1970). Thus, uncertainties in mainshock stress drop estimates are large and our observations do not reject the hypothesis of a high stress drop ($\Delta\sigma > 20\,\text{MPa}$) as is typically observed in the Northeastern US (Viegas et al., 2010).

A particularly active area on the fault plane is down dip and at the northern end of the active fault, where the slip model shows that rupture arrested (Figure 3e). This cluster persists throughout the observation period and locates near the possible intersection with the Ramapo fault (see the red dashed lines in Figure 3c). We therefore interpret the clustered activity as the result of stress concentrations due to a structural heterogeneity acting as a barrier to rupture propagation. We attribute this barrier to a northeast trending strand of the Ramapo fault, which, within the resolution capability of the catalog, does not seem to host any earthquakes.

A b-value of $b = 1.19 \pm 0.03$ (Figure 2b) is significantly larger than 1.0, the global b-value measured with moment magnitudes. Such a high b-value is at odds with the typically large Northeastern US stress drops (Viegas et al., 2010) and the compressional stress regime acting in the Ramapo seismic zone, compression being usually associated with high differential stresses and low b-values (Scholz, 2015; Zaccagnino et al., 2022). Structural properties such as high fault roughness or highly fractured medium could be the cause for the high b-value (Mogi, 1962, 1967; T. H. Goebel et al., 2017). Moreover, the earthquake spatial fall-off rate, $\gamma \approx 1.8$ (Figure 3d), relates to fault roughness and off-fault damage production (Dieterich & Smith, 2010; T. Goebel et al., 2014). Values lower than 2 indicate high roughness (T. Goebel et al., 2014), which is characteristic of immature faults (Perrin et al., 2021). Based on these observations, the Mountainville fault is likely a young, rough and immature fault with low cumulative slip (Perrin et al., 2021), which is also supported by independent observations of poorly coalesced internal structure of slip surfaces in outcrops of the fault zone (Kolawole et al., under review).

5.2 Implications for Seismic Hazard and Local Tectonics

Despite the relatively small effect of the Tewksbury earthquake on society and nearby infrastructure (Boyd et al., 2024), implications for seismic hazard are significant. Although the mainshock broke a relatively small fault area ($A_m \approx 2\,\mathrm{km}^2$), the aftershock sequence activated a significantly larger area (Figure 3d and Figure S4d). The aftershock footprint shows that either a single surface or closely spaced surfaces covering $A_{\mathrm{upper}} \approx 50\,\mathrm{km}^2$ can be activated seismically. Because earthquakes can be complex, multi-fault ruptures (Hamling et al., 2017; Pananont et al., 2017), we speculate that an earthquake of magnitude M_w5.4 to 6.2 for an average stress drop between 1.0 MPa and 20 MPa (Kanamori & Anderson, 1975) is possible, posing a serious risk to the greater New York City metropolitan region. Moreover, one concern is whether intermediate-size earthquakes occurring so close to the misoriented Ramapo fault could trigger significant slip along it, either as a separate event or as part of a complex, multi-fault sequence (Pananont et al., 2017). Thus, if earthquakes within the RSZ mostly nucleate on relatively short, immature faults that are favorably oriented in the contemporary stress field, it is unclear what long-term effects such ruptures have on an old, mature Ramapo fault. Regardless, even a magnitude 5 or 6 on a secondary fault will have significant impact on the greater New York metro region.

Historical seismicity shows that earthquakes of size $M_w > 5$ occur about once every 100 years in Northeastern America (Sykes et al., 2008). The universality of the Gutenberg-Richter law suggests that $M_w > 6$ earthquakes may occur about once every 1000 years. Examples from other stable continental regions – the 2017 M_w6.5 Botswana earthquake (Kolawole et al., 2017; Gardonio et al., 2018) and the 1811-1818 M_w7.0-7.5 New Madrid earthquake sequence (Johnston & Schweig, 1996) – also suggests that the Gutenberg-Richter law does not cut off at lower magnitudes in stable regions than near active continental plate boundaries like in California. It is therefore critical to better understand the processes that drive seismicity along the RSZ and in the rest of the Northeastern US in order to improve our long-term forecast of seismic hazard in this region.

In stable continental regions, where there seems to be no ongoing tectonic deformation above current geodetic measurement noise levels, transient external stress perturbations may play a major role in driving seismicity (Calais et al., 2016). The shallow depth of the mainshock hypocenter, 4.0 km (Figure 3), suggests that the triggering forces were acting from the surface. Hydrological loading, either from direct stress changes caused by variations in the mass of proximal water bodies or indirectly through infiltration of rainwater and increased pore-fluid pressure (Bollinger et al., 2007; Craig et al., 2017; Tarantino et al., 2024), may be among the main drivers of SCR seismicity (Calais et al., 2016; Craig et al., 2017; Daniels & Peng, 2023). A more assertive statement about the triggering forces would require the statistical treatment of an ensemble of earthquakes in the Northeastern US and the modeling of potential triggers (Bollinger et al., 2007).

6 Concluding Remarks

Results from our analysis of the 2024 Tewksbury, NJ, earthquake and its aftershocks emphasize the importance of properly assessing seismic hazard in stable continental regions, especially near metropolitan regions, and, therefore, the necessity to monitor seismic activity. With more than 183,000 entries in the USGS's "Did you feel it" survey, the April 2024 Tewksbury earthquake is the most widely reported event in its history. To improve our generic understanding of seismic hazard in low deformation rate regions (*e.g.*, the maximum earthquake size), it is now important to revisit SCR waveform archives from around the world with modern techniques, such as those used here, in order to mitigate the observational limitations associated with these intrinsically low levels of seismicity. The future of seismicity monitoring in stable continental regions should not only rely on technological developments but must also be accompanied by appropriate investments in instrumentation.

7 Open Research Section

All the seismic data used in this study are available on IRIS at `http://service.iris.edu/fdsnws/dataselect/1/` (last accessed in November 2024). These data were recorded by the seismic networks LD (Lamont Doherty Earth Observatory (LDEO), Columbia University, 1970, DOI: `https://doi.org/10.7914/sn/ld`), GS (Albuquerque Seismological Laboratory (ASL)/USGS, 1980, DOI: `https://doi.org/10.7914/sn/gs`), 4N (Alexandros Savvaidis, 2024, DOI: `https://doi.org/10.7914/5ftj-a296`), PE (Penn State University, 2004, DOI: `https://doi.org/10.7914/sn/pe`) and NE (Albuquerque Seismological Laboratory (ASL)/USGS, 1994, DOI: `https://doi.org/10.7914/sn/ne`). The earthquake catalog was built with the detection and location software BPMF (Beaucé et al., 2024; Beaucé, 2025, v2.0.0-beta2, last accessed in February 2025). The most recent version of BPMF is available at `https://github.com/ebeauce/Seismic_BPMF`. The relocated catalog was built with HypoDD (Waldhauser, 2001, v2.1-beta, last accessed in July 2024). The most recent version of HypoDD is available at `https://github.com/fwaldhauser/HypoDD`. The earthquake catalog is available from the Zenodo repository (Beaucé, 2024, DOI: `https://doi.org/10.5281/zenodo.14058325`). The USGS catalog can be browsed and downloaded at `https://earthquake.usgs.gov/earthquakes/map/` (last accessed November 2024).

Acknowledgments

This work was supported by NSF RAPID grant EAR-2431983. E.B. was funded by the Brinson Foundation. The authors thank Paul Richards for his insightful comments on the manuscript, and thank all who helped deploy stations, and all institutions whose stations made this work possible: USGS, TexNet, Rutgers and Yale universities.

References

Aki, K. (1965). Maximum likelihood estimate of b in the formula log N= a-bM and its confidence limits. *Bull. Earthquake Res. Inst., Tokyo Univ.*, *43*, 237–239.

Aki, K. (1967). Scaling law of seismic spectrum. *Journal of Geophysical Research*, *72*(4), 1217–1231.

Albuquerque Seismological Laboratory (ASL)/USGS. (1980). *US Geological Survey Networks [Dataset].* International Federation of Digital Seismograph Networks. doi: 10.7914/SN/GS

Albuquerque Seismological Laboratory (ASL)/USGS. (1994). *New England Seismic Network [Dataset].* International Federation of Digital Seismograph Networks. doi: 10.7914/SN/NE

Alexandros Savvaidis. (2024). *4N - New Jersey 2024 Earthquake Sequence [Dataset].* International Federation of Digital Seismograph Networks. doi: 10.7914/5FTJ-A296

Al-Ismail, F., Ellsworth, W. L., & Beroza, G. C. (2023). A Time-Domain Approach for Accurate Spectral Source Estimation with Application to Ridgecrest, California, Earthquakes. *Bulletin of the Seismological Society of America*, *113*(3), 1091–1101.

Allmann, B. P., & Shearer, P. M. (2009). Global variations of stress drop for moderate to large earthquakes. *Journal of Geophysical Research: Solid Earth*, *114*(B1).

Armbruster, J. G., & Seeber, L. (1987). The 23 April 1984 Martic earthquake and the Lancaster seismic zone in eastern Pennsylvania. *Bulletin of the Seismological Society of America*, *77*(3), 877–890.

Beaucé, E. (2024, November). *ML-Enhanced catalog of the 5 April 2024 Tewksbury aftershocks [Dataset] .* Zenodo. Retrieved from `https://doi.org/10.5281/zenodo.14058325` doi: 10.5281/zenodo.14058325

Beaucé, E. (2025, February). *ebeauce/Seismic_BPMF: v2.0.0beta2 [Software].* Zenodo. Retrieved from `https://doi.org/10.5281/zenodo.14838292` doi: 10.5281/zenodo.14838292

Beaucé, E., Frank, W. B., Paul, A., Campillo, M., & van Der Hilst, R. D. (2019).

Systematic detection of clustered seismicity beneath the Southwestern Alps. *Journal of Geophysical Research: Solid Earth*, *124*(11), 11531–11548.

Beaucé, E., Frank, W. B., Seydoux, L., Poli, P., Groebner, N., van der Hilst, R. D., & Campillo, M. (2024). BPMF: A Backprojection and Matched-Filtering Workflow for Automated Earthquake Detection and Location. *Seismological Research Letters*, *95*(2A), 1030–1042.

Beaucé, E., Poli, P., Waldhauser, F., Holtzman, B., & Scholz, C. (2023). Enhanced tidal sensitivity of seismicity before the 2019 magnitude 7.1 Ridgecrest, California earthquake. *Geophysical Research Letters*, *50*(14), e2023GL104375.

Beaucé, E., van der Hilst, R. D., & Campillo, M. (2022). Microseismic constraints on the mechanical state of the North Anatolian fault zone 13 years after the 1999 M7.4 Izmit earthquake. *Journal of Geophysical Research: Solid Earth*, *127*(9), e2022JB024416.

Boatwright, J. (1978). Detailed spectral analysis of two small New York State earthquakes. *Bulletin of the Seismological Society of America*, *68*(4), 1117–1131.

Bollinger, L., Perrier, F., Avouac, J.-P., Sapkota, S., Gautam, U., & Tiwari, D. (2007). Seasonal modulation of seismicity in the Himalaya of Nepal. *Geophysical Research Letters*, *34*(8).

Boyd, O. S., Barnhart, W. D., Bourke, J., Chapman, M., Earle, P. S., Huang, G.-c. D., … others (2024). Preliminary Observations of the 5 April 2024 M w 4.8 New Jersey Earthquake. *The Seismic Record*, *4*(4), 240–250.

Brune, J. N. (1970). Tectonic stress and the spectra of seismic shear waves from earthquakes. *Journal of geophysical research*, *75*(26), 4997–5009.

Burroughs, S. M., & Tebbens, S. F. (2001). Upper-truncated power laws in natural systems. *Pure and Applied Geophysics*, *158*, 741–757.

Calais, E., Camelbeeck, T., Stein, S., Liu, M., & Craig, T. (2016). A new paradigm for large earthquakes in stable continental plate interiors. *Geophysical Research Letters*, *43*(20), 10–621.

Clauzet, A., Shalizi, A., & Newman, M. (2009). Power-law distributions in empirical data. *SIAM Rev*, *51*, 661–703.

Craig, T. J., & Calais, E. (2014). Strain accumulation in the New Madrid and Wabash Valley seismic zones from 14 years of continuous GPS observation. *Journal of Geophysical Research: Solid Earth*, *119*(12), 9110–9129.

Craig, T. J., Chanard, K., & Calais, E. (2017). Hydrologically-driven crustal stresses and seismicity in the New Madrid Seismic Zone. *Nature communications*, *8*(1), 2143.

Daniels, C., & Peng, Z. (2023). A 15-year-long catalog of seismicity in the eastern tennessee seismic zone (etsz) using matched filter detection. *Earthquake Research Advances*, *3*(1), 100198.

Delorey, A. A., van der Elst, N. J., & Johnson, P. A. (2017). Tidal triggering of earthquakes suggests poroelastic behavior on the San Andreas Fault. *Earth and Planetary Science Letters*, *460*, 164–170.

Dieterich, J. H., & Smith, D. E. (2010). Nonplanar faults: Mechanics of slip and off-fault damage. *Mechanics, structure and evolution of fault zones*, 1799–1815.

Eshelby, J. D. (1957). The determination of the elastic field of an ellipsoidal inclusion, and related problems. *Proceedings of the royal society of London. Series A. Mathematical and physical sciences*, *241*(1226), 376–396.

Frank, W. B., Shapiro, N. M., Husker, A. L., Kostoglodov, V., & Campillo, M. (2016). Repeating seismicity in the shallow crust modulated by transient stress perturbations. *Tectonophysics*, *687*, 105–110.

Gardonio, B., Jolivet, R., Calais, E., & Leclère, H. (2018). The April 2017 Mw6. 5 Botswana earthquake: an intraplate event triggered by deep fluids. *Geophysical Research Letters*, *45*(17), 8886–8896.

Goebel, T., Candela, T., Sammis, C., Becker, T., Dresen, G., & Schorlemmer, D. (2014). Seismic event distributions and off-fault damage during frictional sliding of saw-cut surfaces with pre-defined roughness. *Geophysical Journal*

International, *196*(1), 612–625.

Goebel, T. H., Kwiatek, G., Becker, T. W., Brodsky, E. E., & Dresen, G. (2017). What allows seismic events to grow big?: Insights from b-value and fault roughness analysis in laboratory stick-slip experiments. *Geology*, *45*(9), 815–818.

Gutenberg, B., & Richter, C. (1941). *Seismicity of the Earth* (Vol. 34). Geological Society of America.

Hamling, I. J., Hreinsdóttir, S., Clark, K., Elliott, J., Liang, C., Fielding, E., … others (2017). Complex multifault rupture during the 2016 Mw 7.8 Kaikōura earthquake, New Zealand. *Science*, *356*(6334), eaam7194.

Han, S., Kim, W.-Y., Park, J. Y., Seo, M.-S., & Kim, Y. (2024). Rupture Model of the 5 April 2024 Tewksbury, New Jersey, Earthquake Based on Regional Lg-Wave Data. *The Seismic Record*, *4*(3), 214–222.

Heki, K. (2003). Snow load and seasonal variation of earthquake occurrence in Japan. *Earth and Planetary Science Letters*, *207*(1-4), 159–164.

Johnson, C. W., Fu, Y., & Bürgmann, R. (2017). Seasonal water storage, stress modulation, and California seismicity. *Science*, *356*(6343), 1161–1164.

Johnston, A. C., & Schweig, E. S. (1996). The enigma of the New Madrid earthquakes of 1811–1812. *Annual Review of Earth and Planetary Sciences*, *24*(1), 339–384.

Kafka, A. L., Schlesinger-Miller, E. A., & Barstow, N. L. (1985). Earthquake activity in the greater New York City area: magnitudes, seismicity, and geologic structures. *Bulletin of the Seismological Society of America*, *75*(5), 1285–1300.

Kanamori, H., & Anderson, D. L. (1975). Theoretical basis of some empirical relations in seismology. *Bulletin of the seismological society of America*, *65*(5), 1073–1095.

Kolawole, F., Atekwana, E. A., Malloy, S., Stamps, D. S., Grandin, R., Abdelsalam, M. G., … Shemang, E. M. (2017). Aeromagnetic, gravity, and Differential

Interferometric Synthetic Aperture Radar analyses reveal the causative fault of the 3 April 2017 Mw 6.5 Moiyabana, Botswana, earthquake. *Geophysical Research Letters*, *44*(17), 8837–8846.

Kolawole, F., Foster-Baril, Z., Seeber, L., Tielke, J., Prakash, A., Colet, M., … Waldhauser, F. (under review). The 2024 M4.8 New Jersey Earthquake: Preferential Seismic Reactivation of a Subtle Immature Rough Fault in Frictionally Unstable Basement Rocks. *Geophysical Research Letters.* doi: 10.1029/2024GL113533

Lamont Doherty Earth Observatory (LDEO), Columbia University. (1970). *Lamont-Doherty Cooperative Seismographic Network [Dataset].* International Federation of Digital Seismograph Networks. doi: 10.7914/SN/LD

Lomax, A., Michelini, A., Curtis, A., Meyers, R., et al. (2009). Earthquake location, direct, global-search methods. *Encyclopedia of complexity and systems science*, *5*, 2449–2473.

Madariaga, R. (1976). Dynamics of an expanding circular fault. *Bulletin of the Seismological Society of America*, *66*(3), 639–666.

Mogi, K. (1962). Magnitude-frequency relation for elastic shocks accompanying fractures of various materials and some related problems in earthquakes. *Bull. Earthq. Res. Inst., Univ. Tokyo*, *40*, 831–853.

Mogi, K. (1967). Earthquakes and fractures. *Tectonophysics*, *5*(1), 35–55.

Ōmori, F. (1894). *On the after-shocks of earthquakes* (Vol. 7). The University.

Page, R. A., Molnar, P. H., & Oliver, J. (1968). Seismicity in the vicinity of the Ramapo fault, New Jersey-New York. *Bulletin of the Seismological Society of America*, *58*(2), 681–687.

Pananont, P., Herman, M., Pornsopin, P., Furlong, K., Habangkaem, S., Waldhauser, F., … others (2017). Seismotectonics of the 2014 Chiang Rai, Thailand, earthquake sequence. *Journal of Geophysical Research: Solid Earth*, *122*(8), 6367–6388.

Penn State University. (2004). *Pennsylvania State Seismic Network [Dataset].* International Federation of Digital Seismograph Networks. doi: 10.7914/SN/PE

Perrin, C., Waldhauser, F., & Scholz, C. H. (2021). The shear deformation zone and the smoothing of faults with displacement. *Journal of Geophysical Research: Solid Earth*, *126*(5), e2020JB020447.

Pomeroy, P. W., Simpson, D. W., & Sbar, M. L. (1976). Earthquakes triggered by surface quarrying-the Wappingers Falls, New York sequence of June, 1974. *Bulletin of the Seismological Society of America*, *66*(3), 685–700.

Powers, P. M., & Jordan, T. H. (2010). Distribution of seismicity across strike-slip faults in California. *Journal of Geophysical Research: Solid Earth*, *115*(B5).

Schaff, D. P., Bokelmann, G. H., Ellsworth, W. L., Zanzerkia, E., Waldhauser, F., & Beroza, G. C. (2004). Optimizing correlation techniques for improved earthquake location. *Bulletin of the Seismological Society of America*, *94*(2), 705–721.

Scholz, C. H. (2015). On the stress dependence of the earthquake b value. *Geophysical Research Letters*, *42*(5), 1399–1402.

Seeber, L., Armbruster, J. G., Kim, W.-Y., Barstow, N., & Scharnberger, C. (1998). The 1994 Cacoosing Valley earthquakes near Reading, Pennsylvania: A shallow rupture triggered by quarry unloading. *Journal of Geophysical Research: Solid Earth*, *103*(B10), 24505–24521.

Seeber, L., Kim, W.-Y., Armbruster, J. G., Du, W.-X., Lerner-Lam, A., & Friberg, P. (2002). The 20 April 2002 Mw 5.0 earthquake near Au Sable Forks, Adirondacks, New York: a first glance at a new sequence. *Seismological Research Letters*, *73*(4), 480–489.

Shearer, P. M. (2019). *Introduction to seismology.* Cambridge university press.

Shi, J., Kim, W.-Y., & Richards, P. G. (1996). Variability of crustal attenuation in the northeastern United States from Lg waves. *Journal of Geophysical Research: Solid Earth*, *101*(B11), 25231–25242.

Shi, J., Kim, W.-Y., & Richards, P. G. (1997). Correction to "Variability of crustal attenuation in the northeastern United States from Lg waves" by Jinghua Shi, Won-Young Kim, and Paul G. Richards. *Journal of Geophysical Research: Solid Earth*, *102*(B6), 11899–11900.

Shi, Y., & Bolt, B. A. (1982). The standard error of the magnitude-frequency b value. *Bulletin of the Seismological Society of America*, *72*(5), 1677–1687.

Sykes, L. R., Armbruster, J. G., Kim, W.-Y., & Seeber, L. (2008). Observations and tectonic setting of historic and instrumentally located earthquakes in the greater new york city–philadelphia area. *Bulletin of the Seismological Society of America*, *98*(4), 1696–1719.

Tarantino, S., Poli, P., D'Agostino, N., Vassallo, M., Festa, G., Ventafridda, G., & Zollo, A. (2024). Non-linear elasticity, earthquake triggering and seasonal hydrological forcing along the Irpinia fault, Southern Italy. *Nature Communications*, *15*(1), 9821.

Utsu, T., Ogata, Y., et al. (1995). The centenary of the Omori formula for a decay law of aftershock activity. *Journal of Physics of the Earth*, *43*(1), 1–33.

Viegas, G., Abercrombie, R. E., & Kim, W.-Y. (2010). The 2002 M5 Au Sable Forks, NY, earthquake sequence: Source scaling relationships and energy budget. *Journal of Geophysical Research: Solid Earth*, *115*(B7).

Waldhauser, F. (2001). *HypoDD-A program to compute double-difference hypocenter locations* (Tech. Rep.).

Waldhauser, F., & Ellsworth, W. L. (2000). A double-difference earthquake location algorithm: Method and application to the northern Hayward fault, California. *Bulletin of the seismological society of America*, *90*(6), 1353–1368.

Waldhauser, F., & Schaff, D. P. (2008). Large-scale relocation of two decades of Northern California seismicity using cross-correlation and double-difference methods. *Journal of Geophysical Research: Solid Earth*, *113*(B8).

White, M. C., Fang, H., Nakata, N., & Ben-Zion, Y. (2020). PyKonal: a Python package for solving the eikonal equation in spherical and Cartesian coordinates using the fast marching method. *Seismological Research Letters*, *91*(4), 2378–2389.

Wiemer, S., & Katsumata, K. (1999). Spatial variability of seismicity parameters in aftershock zones. *Journal of Geophysical Research: Solid Earth*, *104*(B6), 13135–13151.

Wu, P., & Johnston, P. (2000). Can deglaciation trigger earthquakes in N. America? *Geophysical Research Letters*, *27*(9), 1323–1326.

Yang, J.-P., & Aggarwal, Y. P. (1981). Seismotectonics of northeastern United States and adjacent Canada. *Journal of Geophysical Research: Solid Earth*, *86*(B6), 4981–4998.

Zaccagnino, D., Telesca, L., & Doglioni, C. (2022). Scaling properties of seismicity and faulting. *Earth and Planetary Science Letters*, *584*, 117511.

Zhu, W., & Beroza, G. C. (2019). PhaseNet: a deep-neural-network-based seismic arrival-time picking method. *Geophysical Journal International*, *216*(1), 261–273.